Multidiszciplináris Tudományok, 14. kötet, 3. szám (2024) pp. 92-113. **https://doi.org/10.35925/j.multi.2024.3.9**

TEMPERATURE-DEPENDENT SOLID MATERIAL PROPERTIES OF GRCOP-42 FOR AN ADDITIVELY MANUFACTURED LIQUID ROCKET ENGINE LOX COOLING CHANNEL

Nikos Monokrousos
PhD researcher, Cranfield University
Cranfield University, College Road, Cranfield, Bedfordshire, MK43 0AL, United Kingdom, e-mail: nikos.monokrousos@cranfield.ac.uk

László Könözsy
reader/associate professor, Cranfield University
Cranfield University, College Road, Cranfield, Bedfordshire, MK43 0AL, United Kingdom, e-mail: laszlo.konozsy@cranfield.ac.uk

Vassilios Pachidis
professor, Cranfield University
Cranfield University, College Road, Cranfield, Bedfordshire, MK43 0AL, United Kingdom, e-mail: v.pachidis@cranfield.ac.uk

Ernesto Sozio
senior propulsion aerodynamics engineer, Pangea Aerospace
Avinguda Número 1, 20 08040 Barcelona, Spain, e-mail: ernesto.sozio@pangeaaerospace.com

Federico Rossi
head of propulsion, Pangea Aerospace
Avinguda Número 1, 20 08040 Barcelona, Spain, e-mail: federico.rossi@pangeaaerospace.com

Abstract

Recent technological developments in the field of Additive Manufacturing (AM) provide a number of opportunities for the utilisation of high-performance copper alloys for aerospace applications. The additively manufactured LOx/LNG DemoP1 aerospike engine demonstrator designed by Pangea Aerospace is a characteristic example based on the Direct Metal Laser Sintering (DMLS) technology. The aerospike engine thrust chamber and LOx cooling channels are manufactured using GRCop-42 material powder, a Cu-Cr-Nb based copper alloy developed by the National Aeronautics and Space Administration (NASA) for the regenerative cooling technology of high thermal demand thrust chambers and nozzles. In the current work temperature-dependent correlations are derived for the density, specific heat capacity at constant pressure and thermal conductivity of the GRCop-42 material. The correlations for the solid material properties are then introduced into the ANSYS Fluent 2023 R2 Computational Fluid Dynamics (CFD) package and their capabilities are investigated for the characterisation of the flow-field characteristics of the LOx flow in the cooling channel. The numerical solution of the coolant flow in the AM cooling channel is compared against experimental data of the DemoP1 engine demonstrator. The main objective of this study is to provide a realistic physical description of the temperature-dependent properties of the AM solid material in high heat flux applications where the material properties are mostly considered as constant in previous studies.

Keywords: *aerospike engine, additive manufacturing, LOx cooling channel, GRCop-42 copper alloy, material properties*

1. Introduction

In the recent years there has been an intense research effort to develop high-speed propulsion concepts linked to supersonic and hypersonic civil transport, as well as space access applications (Jian and Qiuru, 2020; Tsentis et al., 2023). Most studies focus on computational methods (Weiss et al., 2009; Statnikov et al., 2015), however studies on experimental analyses of such high-speed systems can also be found (Deprés et al., 2004). The majority of the experimental investigations on exhaust nozzle aerodynamics often rely on cold flow tests (Scharnowski and Kähler, 2021; Tsentis et al., 2024) owing to their simpler implementation and reduced cost for the performance of the experimental campaign. While cold flow tests are essential to understand the gas dynamic mechanisms of these applications, the necessity of hot-flow testing lies on providing supplementary information of the heat flux requirements for the determination of the system thermal load management. The increased interest observed for Additive Manufacturing (AM) is directly linked to the technological development of high heat flux applications.

1.1. Additive Manufacturing for aerospace applications

Additive Manufacturing (AM) technologies are currently used for a wide number of high heat flux aerospace applications involving the fabrication of complex metallic components such as combustion chambers and regenerative cooling systems for liquid rocket engines (Gradl et al., 2019). Selective laser melting (SLM) has been a cornerstone process for the additive manufacturing of liquid rocket engine metallic components. Advantages arising from the utilisation of AM technologies for high heat flux aerospace applications regard the reduction of the manufacturing printing time and cost, materials availability and compliance with the minimum requirements for the mechanical and thermophysical material properties (Gradl, 2016). The importance of selecting an appropriate material for the AM technique is crucial for the end-to-end process allowing for the further improvement of the material properties in addition to the development of novel materials targeting on meeting the requirements and demands of specific high heat flux, high pressure propulsion applications (Gradl et al., 2023).

A detailed review of the end-to-end process for the additive manufacturing of liquid rocket engine thrust chambers is found in (Kerstens et al., 2021). In this literature review work the capabilities of metal additive manufacturing for state-of-the-art, high technology readiness level thrust chambers with regenerative cooling systems is reported for multiple manufacturing processes such as the powder bed fusion (PBF) and the directed energy deposition (DED) processes. The advantageous features of AM are strongly highlighted for metallic components of liquid rocket engines, however attention is brought on larger volume components which due to potential scalability limitations redefine the importance of conventional manufacturing techniques. The significance of the laser powder bed fusion (L-PBF) and lased powder directed energy deposition (LP-DED) manufacturing techniques for the characterisation of additively manufactured material properties is also discussed in (Gradl et al., 2023). Following a presentation of the novel alloys developed by the National Aeronautics and Space Administration (NASA) for the improvement of engines performance and cooling capabilities of the AM metallic components for space applications, the significance of the Integrated Computational Materials Engineering (ICME) discipline is reported. Through the integration of ICME in the workflow of the AM processes, computational methods are currently able to provide directions on both the material manufacturing and indications on the physical and mechanical properties of the developed alloy.

The future of additive manufacturing for high heat flux aerospace applications such as the manufacturing of thrust chambers and liquid rocket engine components is prominent with several industrial companies focusing their research and development activities around AM metallic components. The development of the DemoP1, a 20 [kN] thrust liquid oxygen/liquid natural gas (LOx/LNG) aerospike engine demonstrator designed by Pangea Aerospace is an example of how AM unleashes the capabilities of aerospace applications by tackling the manufacturing effort required for complex geometric configurations. A comprehensive review of the AM processes including the fabrication, welding, inspection and machining for the DemoP1 aerospike engine, in addition to details on the full-scale single-injector hot-fire testing campaign are reported in (Rossi et al., 2022). DemoP1 adopts a dual regenerative cooling system for the increased thermal load demands especially encountered at the throat region of the DemoP1 aerospike engine demonstrator. The regenerative cooling system consists of the cooling of the external housing by liquid natural gas and the cooling of the central plug by counterflowing liquid oxygen from the base to the injector plate. For the additive manufacturing of the engine demonstrator the GRCop-42 copper alloy and the Selective Laser Melting (SLM) manufacturing technique were selected. Details on the GRCop-42 solid material are reported in Sec. 1.2. The employed AM process yields large values of non-uniform surface roughness and as a result greater cooling capabilities on penalty of higher pressure drop across the cooling channel (Rossi et al., 2021). Numerical results regarding the engine flow-field and the estimation of the heat transfer and pressure distribution characteristics around the engine demonstrator were presented in (Fadigati et al., 2024). In the current work, a numerical study on the liquid oxygen AM cooling channel of the DemoP1 aerospike engine developed by Pangea Aerospace is presented. The assessment of the constant and temperature-dependent solid material properties of GRCop-42 is performed through the validation of the numerical solutions obtained against experimental data from the hot-fire testing campaign of the DemoP1 engine.

A review of the current role of additive manufacturing (AM) technologies within the space economy and the benefits of AM processes for aerospace applications can be found in (Ghidini et al., 2023). An example is a numerical study of an aircraft heat exchanger designed by means of AM technologies for the evaluation of its heat transfer capabilities and pressure drop characteristics. The configuration is then compared against a conventionally fabricated heat exchanger of similar geometry (Saltzman et al., 2018). The results indicated the increased heat transfer capabilities of the AM configuration for the thermal load demands of the heat exchanger with the penalty however of an approximately double pressure drop, as a result of the high and non-uniform, process-induced material surface roughness.

1.2. GRCop-42 material properties

Recent advances in Additive Manufacturing (AM) for high-performance propulsion applications indicate copper-based alloys as ideal candidates due to the high thermal conductivity and the excellent mechanical properties of the materials (Morshed-Behbahani et al., 2024). A preliminary conceptualisation for the utilisation of a cold-sprayed Cu-4 at.%Cr-2 at.%Nb copper-based alloy for high heat flux applications was conceived in (Li et al., 2006). The investigation of Li et al. (Li et al., 2006) indicated the GRCop-42 copper alloy material as a promising potential candidate for the manufacturing of combustion chambers with a regenerative cooling system due to the high thermal conductivity and temperature strength of the alloy. Following the full characterisation of the GRCop-84 material properties and AM build parameters (Gradl et al., 2017), the process development and the determination of the initial properties of GRCop-42 for aerospace applications was demonstrated in (Gradl et al., 2019). The reduction of the GRCop-84 alloying elements quantity in half resulted in the new copper alloy GRCop-42 with higher thermal conductivity while retaining the advantageous

mechanical properties of its predecessor (Ellis, 2004). The superiority of superalloys in comparison with copper alloys in terms of mechanical strength is profound, however the higher thermal conductivity of the latter is crucial for high pressure applications which stress the wall temperature limits of the material.

In the recent years increased interest has been demonstrated on the utilisation of GRCop-42 in comparison with GRCop-84 for the manufacturing of combustion chamber liners for rocket engines due to the high thermal conductivity and the development of the supply chain for additive manufacturing applications (Demeneghi et al., 2021). This improvement of thermal conductivity for the GRCop-42 is attributed to the lower concentrations of chromium and niobium in the alloy composition (Gradl et al., 2019). A summary describing the process followed for the production of fully-functional 3D printable GRCop-42 is found in (Cooper et al., 2018). In the technical memorandum published by NASA the advantages of GRCop-42 in comparison with the GRCop-84 were presented in terms of both mechanical properties and 3D printing time. Both alloys belong to the Glenn Research Copper (GRCop) family, else identified as precipitation-hardened (PH) Cu-Cr-Nb alloys (Morshed-Behbahani et al., 2024).

A number of additive manufacturing techniques can be employed for the manufacturing of the GRCop-42 material. The characteristics of the copper alloy manufactured using the powder bed fusion (PBF) technique were demonstrated in (Gradl et al., 2019). Following this study, the quantification of the size effects on the microstructure and the mechanical characteristics of additively manufactured GRCop-42 using the laser powder bed fusion technique was exhibited in (Demeneghi et al., 2021). In this study the influence of different surface parameters such as roughness, porosity and microstructure on the mechanical properties of GRCop-42 was investigated for different values of build wall thickness. Their work clearly demonstrated the significant effect of reducing wall thickness on the porosity of GRCop-42 rather than on the roughness and the microstructure characteristics of the copper alloy. The PBF manufacturing technique however demands additional material powder and imposes limitations on the scalability of the printed component (Gibson et al., 2015). The drawbacks of the PBF technique can be overcome with the directed energy deposition (DED) process, which results in an extension of the component scalability in addition to a reduction in the material required for the manufacturing of the AM component. An investigation on the capabilities of the DED technique as an alternative to the PBF process and other conventional manufacturing processes was exhibited in (Landes et al., 2020). The work of Jasthi et al. (Jasthi et al., 2023) focused on the evaluation of the microstructure and mechanical properties of the GRCop-42 copper-based alloy developed through a cold-spray process under high pressure values for the manufacturing of the combustion chamber liners of rocket engines. The utilisation of a cold-spray process bypasses the drawbacks of the PBF technique related to the structural properties of the manufactured material and results in advantageous features for high heat flux aerospace applications. A comprehensive review of different additive manufacturing techniques for copper-chromium-niobium alloys can be found in (Tang et al., 2022). In (Morshed-Behbahani et al., 2024) details on the AM processes, post-printing strategies and standardization and certification procedures required for the manufacturing of metallic components from copper-based alloys are reported.

Copper alloys are employed for various applications at cryogenic temperatures requiring high material conductivity and mechanical strength. For instance, a complete guide for the physical and mechanical material properties of oxygen-free copper, beryllium copper and phosphor bronze can be found in (Simon et al., 1992). A plethora of experimental data and correlations describing the thermophysical properties of metal elements are available in the literature. Measurements for the determination of the density of copper with respect to temperature ranging from 293 [K] up to the critical temperature of copper equal to 8900 [K] can be found in (Cahill and Kirshenbaum, 1962). A molecular dynamic-based modelling of the thermophysical properties of copper is presented in (Demin et al.,

2020). Lastly the construction of equations of state based on experimental measurements for the thermodynamic properties of solid and liquid copper in a temperature range varying from 20 [K] up to 3900 [K] can be found in (Kozyrev, 2023). The characterisation for the density of the steel alloying metals in both the solid and liquid state for chromium and niobium was presented in (Thurnay, 1998). In this work polynomial coefficients in a wide range of temperatures are reported and employed for the solution of the temperature-dependent polynomials and the estimation of the transition metals density. The temperature-dependent correlations for the determination of the specific heat capacity at constant pressure property of copper, chromium and niobium were presented in (National Institute of Standards and Technology, 2023) and the coefficients employed for the solution of the reported formulations are based on the work of (Chase, 1998). In addition, the specific heat capacity at constant pressure and volume of copper for temperatures ranging from 1 [K] to 1300 [K] are found in (White and Collocott, 1984). For the determination of a polynomial reference equation for the specific heat capacity at constant pressure, different coefficients are introduced with respect to the examined temperature-range of copper material. Experimental data for the thermal conductivity of the pure elements of copper, chromium and niobium over a wide temperature range are available in (Ho et al., 1972). The reliability range and the error estimates for the utilisation of the experimental data for each element are also reported. Pure copper measurements are indicated as accurate within a range of ±4% for low and high temperatures whilst the range reduces to ±2% near room temperature. The experimental measurements for chromium are accurate within ±3% for temperatures ranging from 150 [K] to 700 [K] and ±10% for temperatures below 150 [K]. Lastly, the thermal conductivity data available in (Ho et al., 1972) for pure niobium are accurate within ±15% for low and high temperatures and ±5% to ±10% for moderate temperatures.

As discussed, the GRCop-42 copper alloy consists of Cu-4 at.%Cr-2 at.%Nb and a number of elements such as Fe, O, Al and Si in small weight percentages. Chromium and niobium alloying yields in the formation of Cr_2Nb particles which enhance the strengthening mechanical properties of the material in high temperatures. The main drawback of the chromium-niobium alloying which constitutes the basis of the GRCop-42 copper alloy is the magnification of the resulting particles as temperature decreases during cooling processes (Ellis, 2005). The literature available for the thermophysical properties of the GRCop-42 is limited. A number of thermodynamic and mechanical properties of the copper-based alloys GRCop-42 and GRCop-84 can be found in (Gradl et al., 2019). Experimental measurements for GRCop metallic parts manufactured with different systems and parameters regarding properties such as the specific heat capacity at constant pressure, thermal conductivity and thermal expansion are available in (Chen et al., 2023). The present work aims to present correlations for the determination of density, specific heat capacity at constant pressure and thermal conductivity of the GRCop-42 copper alloy based on regression models fitting the experimental data and expressions available for the individual alloying metals. The assessment of the resulted temperature-dependent solid material properties is performed through the validation of the numerical solution for liquid oxygen in the AM cooling channel of the DemoP1 aerospike engine designed by Pangea Aerospace.

2. Methodology

In this section, the governing equations for the solution of liquid oxygen in the Additively Manufactured (AM) cooling channel of the DemoP1 aerospike engine demonstrator are presented, in addition to the numerical implementation details into the commercial Computational Fluid Dynamics (CFD) package. A grid sensitivity analysis is also presented for the determination of an appropriate grid size. In Sec. 3

the results of the numerical simulation of liquid oxygen in the AM cooling channel and evidence for the performance of the temperature-dependent solid material properties of GRCop-42 are provided.

2.1. Governing equations

For the numerical solution of liquid oxygen in the Additively Manufactured (AM) cooling channel of the DemoP1 aerospike engine demonstrator specific numerical activities have been performed. The geometric configuration of interest is a three-dimensional curved channel of rectangular, variable cross-section for the reduction of the fluidic width and the satisfaction of the increased heat transfer demands at the throat region of the AM cooling channel (Rossi et al., 2021). The three-dimensional model includes the inlet and outlet section in addition to the surrounding wall boundaries. The thermal load from the hot-gas side is applied on the geometric configuration through the bottom (basement) wall of the liquid oxygen cooling channel. The system of the governing equations for steady-state consists of the mass conservation (continuity), momentum and energy equations. Assuming no external forces are acting on the fluid body, the governing equations solved in the case of the three-dimensional model read

$$\frac{\partial}{\partial x_i}(\rho u_i) = 0, \tag{1}$$

$$\frac{\partial}{\partial x_j}(\rho u_i u_j) = -\frac{\partial P}{\partial x_i} + \frac{\partial}{\partial x_j}\left[\mu\left(\frac{\partial u_i}{\partial x_j} + \frac{\partial u_j}{\partial x_i} - \frac{2}{3}\delta_{ij}\frac{\partial u_i}{\partial x_j}\right)\right] + \frac{\partial}{\partial x_j}\left(-\rho\overline{u_i' u_j'}\right), \tag{2}$$

$$\frac{\partial}{\partial x_j}[u_i(\rho E + p)] = \frac{\partial}{\partial x_j}\left[\left(\lambda + \frac{c_p \mu_t}{Pr_t}\right)\frac{\partial T}{\partial x_j} + u_i\left(\tau_{ij}\right)_{eff}\right], \tag{3}$$

where $i, j = 1, 2, 3$ indicates the three coordinate directions, u_i is the velocity component in the corresponding coordinate direction, ρ is the density of the fluid, P the static pressure, μ the dynamic viscosity of the fluid, δ_{ij} is the Kronecker delta, E is the total energy defined as $E = c_p T - \frac{p}{\rho} + \frac{u^2}{2}$, λ is the thermal conductivity, c_p is the specific heat capacity at constant pressure, μ_t is the turbulent (eddy) dynamic viscosity, Pr_t is the turbulent Prandtl number, T is the static temperature of the fluid and $\left(\tau_{ij}\right)_{eff}$ is the deviatoric stress tensor defined as

$$\left(\tau_{ij}\right)_{eff} = \mu_{eff}\left(\frac{\partial u_j}{\partial x_i} + \frac{\partial u_i}{\partial x_j}\right) - \frac{2}{3}\mu_{eff}\frac{\partial u_i}{\partial x_j}\delta_{ij}, \tag{4}$$

for $i, j = 1, 2, 3$ and $j \neq i$. For the numerical solution of liquid oxygen- in the AM cooling channel of the DemoP1 aerospike engine the following boundary conditions are employed: at the inlet section a fixed mass flow rate equal to the experimentally measured values of $\dot{m} = 0.076$ [kgs^{-1}] and a uniform temperature profile $T = T_{in} = 107.4$ [K] are imposed, at the outlet section a pressure outlet condition employed is equal to the measured value $P = P_{out} = 57.09$ [bar]. The accuracy of the temperature sensors is reported to be ±7 [K] while the accuracy of the pressure sensor ±0.8 [bar].

At the channel walls, no-slip boundary conditions are employed for the rough surfaces with the roughness height set equal to $k_s = 59.17$ [μm] and the roughness constant equal to 0.75, to account for the non-uniform distribution of the rough elements induced by the AM process. For the roughness modelling, the standard roughness option on the commercial CFD package was selected. The roughness

height assigned to the wall boundaries of the AM cooling channel has been set equal to the equivalent sand-grain roughness estimated based on the statistical surface roughness parameters obtained from an optical profilometry process on the metallic components of the DemoP1 aerospike engine demonstrator. The heat flux is set equal to zero for all wall boundaries except for the bottom (basement) wall. As discussed, the heat load from the hot-gas side of the DemoP1 through the GRCop-42 solid material to the coolant side where liquid oxygen flows is applied through the basement wall of the AM cooling channel. Subsequently to the estimation of the heat transfer coefficient and heat transfer rate from the hot-gas side to the wall material, the one-dimensional Fourier equation for the heat conduction was solved and a temperature profile at the coolant-side wall was obtained. The hot-gas side wall temperature is assumed to be uniform and equal to $T_{w,hg} = 800$ [K]. To accurately capture the coolant-side wall temperature profile of the liquid oxygen AM cooling channel, the profile was split into three intervals and different regression models were employed to fit the curve of the temperature profile.

Table 1. *Regression model characteristics for curve fitting of coolant-side wall temperature profile.*

	Regression model	Number of terms	R^2	Root-mean-square error (RMSE)
Interval 1	Fourier	4	0.9999	0.01277
Interval 2	Fourier	8	0.9981	0.5574
Interval 3	Fourier	4	0.9999	0.01277

The regression model characteristics for the fitting of the coolant-side wall temperature profile were obtained from the Curve Fitter toolbox of MATLAB R2022a (The Mathworks, 2020) and are summarised in Table 1. Following the determination of the regression models and their statistical characteristics for each interval, the resulted coolant-side wall temperature profile from the one-dimensional Fourier's law for heat conduction in addition to the fit curve obtained from the employed regression models can be seen in Fig. 1. The obtained correlation for the determination of the coolant-side wall temperature with respect to the longitudinal coordinate of the AM cooling channel was implemented as a User-Defined Function (UDF) and integrated in the commercial CFD package as a thermal boundary condition for the basement wall of the liquid oxygen cooling channel.

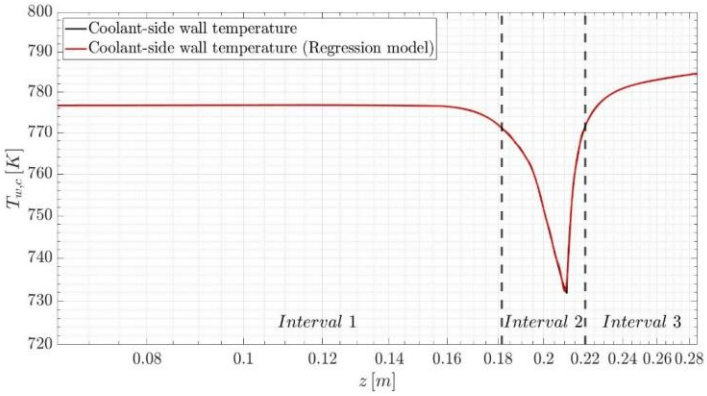

Figure 1. *Coolant-side wall temperature profile and regression model for its curve fit.*

2.2. Numerical implementation details

The numerical simulations for the solution of the liquid oxygen flow in the AM cooling channel of the DemoP1 aerospike engine are performed in the commercial CFD package ANSYS Fluent 2023 R2 (ANSYS, 2023). For the closure of the Reynolds-Averaged Navier-Stokes (RANS) problem the turbulence model selected is the $k-\omega$ shear stress transport (SST) model (Menter, 1994). The benefit arising from the utilisation of the $k-\omega$ SST model is the combination of solving the near-wall region with the standard $k-\omega$ turbulence model and the outer region using the $k-\varepsilon$ model (Menter, 2009). The advantageous features of the $k-\omega$ SST turbulence model for the numerical solution of internal turbulent flows in rough channels have been exhibited in previous studies (Ricci, et al., 2016). The transport equations for the $k-\omega$ SST turbulence model (Menter, 1994) are written as

$$\frac{\partial}{\partial t}(\rho k)+\frac{\partial}{\partial x_i}(\rho k u_i)=\frac{\partial}{\partial x_j}\left[\left(\mu+\frac{\mu_t}{\sigma_k}\right)\frac{\partial k}{\partial x_j}\right]+\tilde{G}_k-Y_k+S_k, \tag{5}$$

$$\frac{\partial}{\partial t}(\rho \omega)+\frac{\partial}{\partial x_i}(\rho \omega k u_i)=\frac{\partial}{\partial x_j}\left[\left(\mu+\frac{\mu_t}{\sigma_\omega}\right)\frac{\partial \omega}{\partial x_j}\right]+G_\omega-Y_\omega+D_\omega+S_\omega, \tag{6}$$

where k is the turbulence kinetic energy, ω the specific dissipation rate, $\tilde{G}_k$ is turbulence kinetic energy production and G_ω the specific dissipation rate generation, Y_k and Y_ω represent the turbulence dissipation term and S_k and S_ω the source terms of the transport equations. The D_ω term in the transport equation for the specific dissipation rate of the $k-\omega$ SST turbulence model in Eq. 6 constitutes the cross-diffusion term which integrates the blending function of the model. Details on the model parameters and the implementation of the $k-\omega$ SST turbulence model are found in (Menter, 1994).

The simulations for the liquid oxygen in the AM cooling channel of the DemoP1 aerospike engine are obtained using a three-dimensional computational fluid dynamics (CFD) approach. The numerical solution is based on an implicit, density-based method for the steady-state compressible Reynolds-Averaged Navier-Stokes equations in conjunction with the $k-\omega$ SST turbulence model (Menter, 1994). The fluid material density is determined based on the ideal gas law, the specific heat capacity at constant pressure using a fifth-order piecewise polynomial with respect to the static temperature, the thermal conductivity of the fluid is determined based on the kinetic theory and the dynamic viscosity estimation relies on Sutherland's law. The AM cooling channel of the DemoP1 engine has been manufactured using the copper-alloy GRCop-42 which is currently unavailable on ANSYS Fluent. For this reason, the solid material properties of the copper alloy are introduced either as constants or through the implementation of User-Defined Functions (UDFs) for the expressions obtained from the analysis presented in Sec. 3.1. The reference values of the fluid material are computed from the inlet section of the cooling channel. For the discretisation of the convective fluxes, the Roe Approximate Riemann Solver (ARS) was employed (Roe, 1981), whilst second-order accurate upwind schemes are employed for the flow variables and the transport quantities of the $k-\omega$ SST turbulence model. The absolute criteria for the convergence of the continuity, velocity components and the transport quantities of the turbulence model are set equal to 10^{-8} and the convergence criterion for the energy is set as 10^{-12}. The standard initialisation method is employed and the solution is initialised from the inlet section in a reference frame relative to the cell zone. The simulations have been performed for a total number of 10^4 iterations.

A grid refinement study has been performed for the investigation of the numerical solution sensitivity on the grid size. The total number of cells for the coarse, intermediate and fine grid employed is reported

in Table 2. The grid convergence test case is made for the numerical simulation where solid material properties for the copper-based alloy GRCop-42 are assumed to be constant with temperature.

Table 2. *Number of cells for the grids investigated in the grid refinement study.*

	Number of cells
Grid A (coarse)	0.87M
Grid B (intermediate)	1.3M
Grid C (fine)	2.6M

The results are presented in terms of a temperature profile at the outlet section of the liquid oxygen AM cooling channel at the midline from the heated bottom wall (basement) up to the adiabatic top wall boundary. Small deviations are observed in Fig. 2 between the temperature profiles obtained for the coarse, intermediate and fine grid investigated. The displacement of Grid A in comparison with the intermediate and the fine grid is justified based on the coarseness of the grid. The mean error percentage computed between the temperature values obtained from the numerical solution with Grid A (coarse) and Grid C (fine) is 2.765%. The mean variation reported between the numerical results obtained with Grid B (intermediate) and Grid C (fine) is estimated as 1.205% which justifies the selection of the fine grid for the performance of the required numerical simulations.

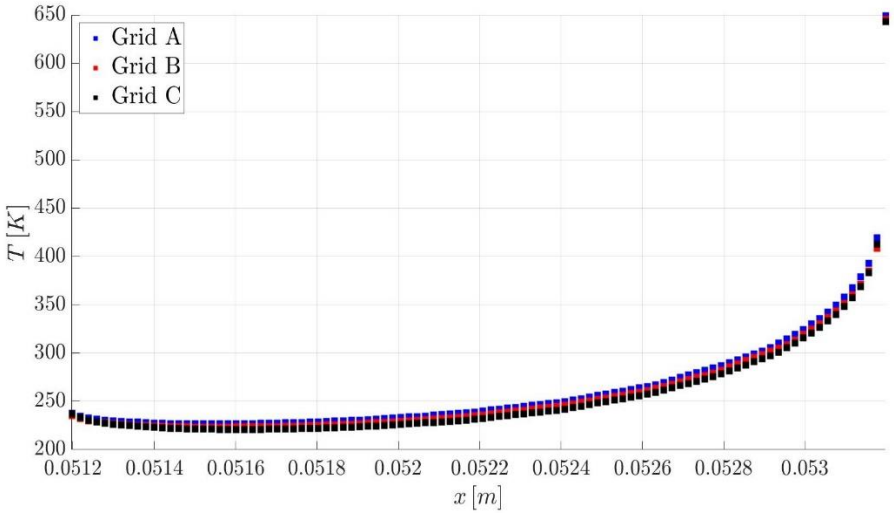

Figure 2. *Grid sensitivity analysis for the temperature profile at the basement-top wall midline of the outlet section of the AM cooling channel.*

3. Results and discussion

In this section, the results of the numerical simulations performed for the solution of liquid oxygen in the Additively Manufactured (AM) cooling channel of the DemoP1 aerospike engine demonstrator are reported. The differentiation of the performed simulations regards the properties of the solid material. Two different approaches are investigated: the imposition of constant material properties for the

GRCop-42 alloy in standard room temperature (298.2 [K]) and the implementation of User-Defined Functions (UDFs) for the assessment of the temperature-dependent correlations for the density, specific heat capacity at constant pressure and thermal conductivity of the copper alloy used for the manufacturing of the engine demonstrator. Following the derivation of the temperature-dependent solid material properties of the alloy GRCop-42, the numerical solutions obtained with the different type of solid material properties are validated against measured data available from the experimental campaign of the DemoP1 engine. The numerical simulations have been performed in the commercial CFD package ANSYS Fluent 2023 R2 on an Intel(R) Core(TM) i7-10700 at 2.90 GHz computer with 32GB RAM.

3.1. Temperature-dependent solid material properties for GRCop-42

In the current work temperature-dependent correlations for the thermophysical properties of the copper-based alloy GRCop-42 are presented. The density, specific heat capacity at constant pressure and thermal conductivity solid material properties are based on the individual corresponding properties of copper, chromium and niobium which constitute the examined alloy. As discussed, GRCop-42 consists of Cu-4 at.%Cr-2 at.%Nb and pure elements such as Fe, O, Al and Si in smaller percentages. Details on the powder chemistry of GRCop-42 (Gradl et al., 2019) can be seen in Table 3.

Table 3. *Powder chemistry of GRCop-42 copper-based alloy (Gradl et al., 2019).*

Element	GRCop-42 Wt%
Cr	3.1 – 3.4
Nb	2.7 – 3.0
Fe	< 50 ppm
O	< 400 ppm
Al	< 50 ppm
Si	< 50 ppm
Cu	Balance

For the derivation of temperature-dependent solid material properties for the GRCop-42 copper alloy an average weight percentage concentration based on the details presented in Table 3. is assumed for chromium to be 3.25 Wt% and niobium equal to 2.85 Wt%. Other elements (Fe, O, Al and Si) constituting the copper-alloy are not considered for the estimation of the thermophysical properties of GRCop-42. The remaining weight of GRCop-42 is balanced by the concentration of pure copper which is estimated to be equal to 93.9 Wt%. The investigated temperature-dependent properties are weight-averaged and estimated based on the weight percentage of each alloying pure element as

$$x = w_{Cu}x_{Cu} + w_{Cr}x_{Cr} + w_{Nb}x_{Nb}, \quad (7)$$

where x is the investigated temperature-dependent property of the solid material and w represents the average Wt% of each alloying metal in the composition of GRCop-42 given as $w_{Cu} = 0.939$, $w_{Cr} = 0.0325$ and $w_{Nb} = 0.0285$. The density values of copper are estimated based on the correlation obtained from experimental data available in the literature (Cahill and Kirshenbaum, 1962) and the density of chromium and niobium is determined from (Thurnay, 1998). Based on the weighted-average process with respect to the weight percentages of each alloying metal, the density of GRCop-42 is estimated based on Eq. 7 and a regression model is employed to fit and extract the temperature-dependent correlation for the corresponding property. The regression model selected is a first-order polynomial characterised by $R^2 = 1.0$ and $RMSE = 0.3869$. The resulted temperature-dependent density reads

$$\rho_w = a_o T_w + a_1, \quad (8)$$

where $a_0 = -0.7636$ and $a_1 = 9005$. The units of the density correlation are [kgm^{-3}]. The mean error between the density formulation for GRCop-42 obtained from the weighted-average process from Eq. 7 and the regression model employed to fit the resulted curve in Eq. 8 is estimated to be equal to 0.00353% in the temperature range 1 [K] to 1300 [K] and 0.00271% in the temperature range of interest in the application of the liquid oxygen flow in the AM cooling channel of the DemoP1 aerospike engine between 298 [K] and 1000 [K]. The temperature-dependent density of the alloying metals in addition to the weighted-average and the proposed correlation for GRCop-42 in Eq. 8 is seen in Fig. 3.

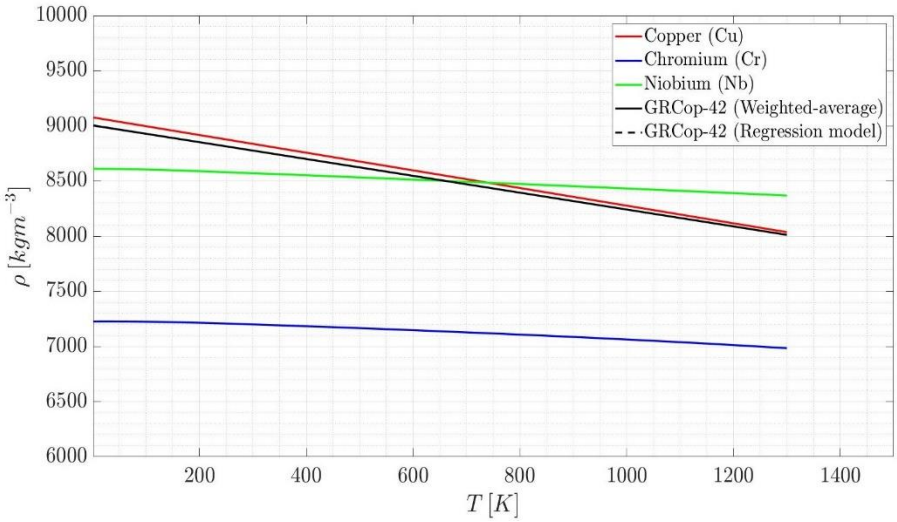

Figure 3. *Temperature-dependent density of GRCop-42 and its alloying metals (Cu, Cr, Nb).*

The derivation of the temperature-dependent specific heat capacity at constant pressure and thermal conductivity correlations of the copper-based alloy GRCop-42 is performed in a similar manner. The solid phase heat capacity at constant pressure for copper, chromium and niobium is evaluated from the Sohmate equation available in (National Institute of Standards and Technology, 2023) and is based on the coefficients extracted from the work of Chase (Chase, 1998). Following the weighted average process according to the weight percentage of the alloying metals in the composition of GRCop-42 from Eq. 7, the regression model selected to fit the curve is a two-term power regression model characterised

by $R^2 = 1.0$ and $RMSE = 52.23$. The resulted temperature-dependent correlation for the specific heat capacity at constant pressure for GRCop-42 is written as

$$c_{p,w} = a_2 T_w^{a_3} + a_4, \tag{9}$$

where $a_2 = 1.086 \times 10^6$, $a_3 = -2.002$ and $a_4 = 408.8$. The units of the specific heat capacity at constant pressure correlation are [Jkg^{-1}K^{-1}]. The mean deviation between the formulation for the specific heat capacity at constant pressure for GRCop-42 obtained from the weighted-average process described in Eq. 7 and the employed regression model reported in Eq. 9 is equal to 8.92% for temperatures ranging from 1 [K] to 1300 [K] and 4.346% in the temperature range of interest to the presented application (298 [K] to 1000 [K]). The temperature-dependent specific heat capacity at constant pressure for GRCop-42 in Eq. 9 in addition to its alloying metals is displayed in Fig. 4.

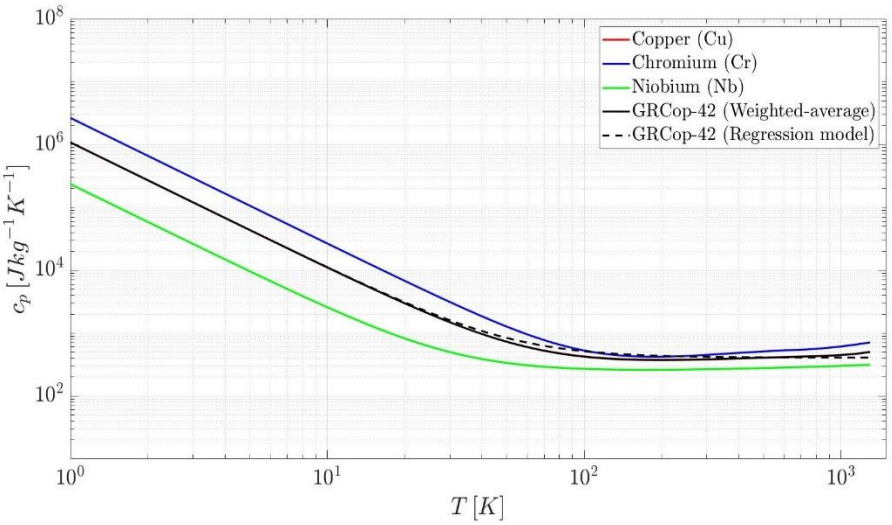

Figure 4. *Temperature-dependent specific heat capacity at constant pressure of GRCop-42 and its alloying metals (Cu, Cr, Nb).*

Lastly, experimental data for the thermal conductivity of copper, chromium and niobium are available in (Ho et al., 1972). Similarly to the derivation of temperature-dependent correlations for the density and specific heat capacity at constant pressure of GRCop-42, a regression model is employed to fit the resulted curve of the weighted-average process based on the weights of the alloying metals in the composition of the copper-based alloy as described in Eq. 7. The selected regression model is a fourth-order Gaussian fit characterised by $R^2 = 0.9987$ and $RMSE = 316.5$. The temperature-dependent correlation for the description of the GRCop-42 thermal conductivity reads

$$k_w = \sum_{i=1}^{4} b_i e^{-\left(\frac{T_w - c_i}{d_i}\right)^2}. \tag{10}$$

The coefficients for Eq. 10 are summarised in Table 4.

Table 4. *Coefficients of fourth-order Gaussian fit for thermal conductivity correlation of GRCop-42 material.*

	b_i	c_i	d_i
$i = 1$	1.404×10^4	6.796	4.891
$i = 2$	1.302×10^4	12.82	7.552
$i = 3$	4556	24.51	15.08
$i = 4$	745	−3807	5431

The units of the thermal conductivity of the GRCop-42 material are [$Wm^{-1}K^{-1}$]. The mean error between the weighted average correlation for the thermal conductivity of GRCop-42 in Eq. 7 and the correlation resulted from the selected regression model in Eq. 10 is equal to 8.268% for temperatures between 1 [K] and 1300 [K] and 6.297% in the temperature range from 298 [K] to 1000 [K]. The extracted temperature-dependent thermal conductivity of the GRCop-42 from Eq. 10 and the alloying metals comprising it is exhibited in Fig. 5. For consistency the small step at $T = 7$ [K] on the experimental data available for the thermal conductivity of chromium (Ho et al., 1972) was not excluded.

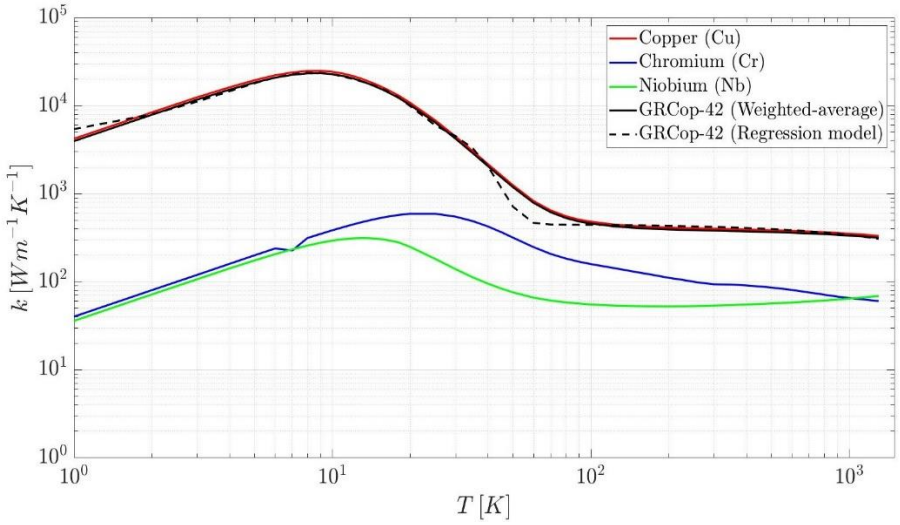

Figure 5. *Temperature-dependent thermal conductivity of GRCop-42 and its alloying metals (Cu, Cr, Nb).*

For the utilisation of distinct experimental values of thermophysical properties to derive temperature-dependent correlations, the employment of regression models for data fitting is required. The reason is that the implementation of the temperature-dependent correlations on a commercial CFD package through User-Defined Functions (UDFs) requires a formulation of the examined property with respect to the static temperature over a continuous range of values. This approach introduces additional uncertainty to the numerical solution and it nevertheless should be performed with attention.

3.2. Numerical results

For the assessment of the derived temperature-dependent correlations for the thermophysical properties of the copper-based alloy GRCop-42, the numerical solution for the liquid oxygen in the AM cooling channel of the DemoP1 aerospike engine demonstrator is compared against experimental data obtained from the performed hot-flow test. As discussed, two different approaches are investigated. The first one regards setting constant with temperature solid material properties for the GRCop-42 alloy in the standard room temperature 298.2 [K]: $\rho_w = 8777.387$ [kgm^{-3}], $c_{p,w} = 383.841$ [Jkg^{-1}K^{-1}] and $k_w = 381.121$ [Wm^{-1}K^{-1}]. The second approach relies on the implementation of the temperature-dependent correlations for the solid material properties described in Eqs. 8-10 in the form of a User-Defined Function (UDF) and their integration into the commercial CFD package. The geometric configuration of the AM channel cooling the central plug of the DemoP1 aerospike engine demonstrator by counterflowing liquid oxygen from the base up to the injector plate is seen in Fig. 6.

Figure 6. *Geometric configuration of liquid oxygen additively manufactured (AM) cooling channel of the DemoP1 aerospike engine demonstrator developed by Pangea Aerospace.*

The assessment of the numerical solution for the liquid propellant flow in the AM cooling channel of the aerospike engine demonstrator is performed against the experimental measurement for the coolant temperature at the outlet section of three-dimensional channel. According to the performed hot-flow test, the measured temperature value at the outlet section of the AM cooling channel is equal to $T_{out} = 305.07$ [K]. In Fig. 7 the average bulk temperature in different cross-sections of the cooling channel is presented. Note that the inlet section of the AM cooling channel is depicted at the right of the figures presented in this analysis whilst the outlet section at the left-side. Both the numerical simulation of liquid oxygen employing constant solid material properties for the GRCop-42 material and the simulation under the assumption of temperature-dependent properties of the copper alloy exhibit similar trends: the coolant enters the AM cooling channel in a cryogenic temperature of $T_{in} = 107.404$ [K] and increases its bulk temperature as it counterflows across the channel surrounding the chamber from the base to the injector plate of the aerospike engine demonstrator. The slope of the temperature gain is steeper across the throat region comparing to the remaining sections of the AM cooling channel. To understand and quantify the steepness of the throat region in comparison with the rest of the cooling channel, the average slope value inside the throat is 1876.85 whilst the average slope from the inlet section to the throat is computed as 460.42 and from the exit of the throat up to the outlet section as 573.58. This temperature gradient at the throat region is expected in the application of the DemoP1 aerospike engine demonstrator

due to the aerospike engine geometric configuration and the higher heat flux from the hot-gas side to the coolant side applied at the throat region. After exiting the throat, the bulk temperature of the coolant increases until it reaches the outlet section of the AM cooling channel. The results of the performed simulations indicate identical results in terms of averaged values across the examined channel cross-sections for each variable of interest, such as total temperature, static pressure, total velocity and density of the fluid. More specifically the temperature gain for both the cases where constant with temperature and temperature-dependent solid material properties were employed for the GRCop-42 copper alloy material at the wall boundaries of the AM cooling channel is computed to be equal to 191.722 [K].

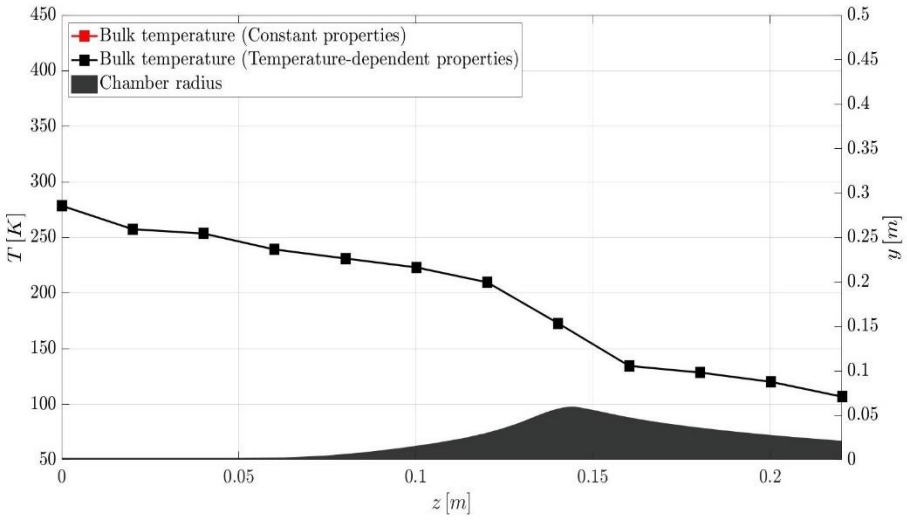

Figure 7. *Average bulk temperature at different cross-sections across longitudinal coordinate of coolant side for constant and temperature-dependent solid material properties.*

Following the estimation of an average value for temperature at the outlet section of the AM cooling channel, the resulted values can be compared against the measured value obtained from the hot-fire testing experimental campaign of the DemoP1 aerospike engine demonstrator. The experimental measurement from the hot-flow test of the aerospike engine is $T_{out,exp} = 305.07$ [K]. In both simulations performed the computed average temperature at the outlet section of the cooling channel is $T_{out} = 299.173$ [K] and the percentage difference with respect to the experimental value is 1.933%, which is acceptable. The results indicate that the employment of temperature-dependent solid material properties of GRCop-42 also allows for the proper determination of the flow-field characteristics for the liquid oxygen in the AM cooling channel, in addition to considering constant solid material properties at the wall boundaries as reported in previous studies (Pizzarelli et al., 2013; Betti et al., 2014).

In Fig. 8 the average coolant static pressure in different cross-sections across the cooling channel is presented. The characteristics of the pressure-field are similar in both cases: the coolant enters the AM channel at high pressure and a small pressure drop is immediately observed up to the beginning of the throat region. The results indicate an adverse pressure drop within the throat region until the coolant exits the throat, where its pressure reduces in a smoother way up to the outlet section of the cooling channel. Similar to the case of the characterisation of the bulk temperature of the fluid, identical results were produced for the pressure-field across the AM cooling channel of the aerospike engine demonstrator. In the case of both the constant and temperature-dependent GRCop-42 solid material

properties the pressure drop across the cooling channel is estimated to be equal to 161.014 [bar]. Note that the pressure drop from the inlet section of the cooling channel up to the beginning of the throat region is approximately 3 [bar] whereas the pressure drop from the inlet section up to the exit of the throat is around 115 [bar]. This indicates that most of the total pressure drop is happening by the time the coolant exits the throat region, considering that this amount accounts for almost 70% of the total pressure drop in the additively manufactured cooling channel of the DemoP1 aerospike engine.

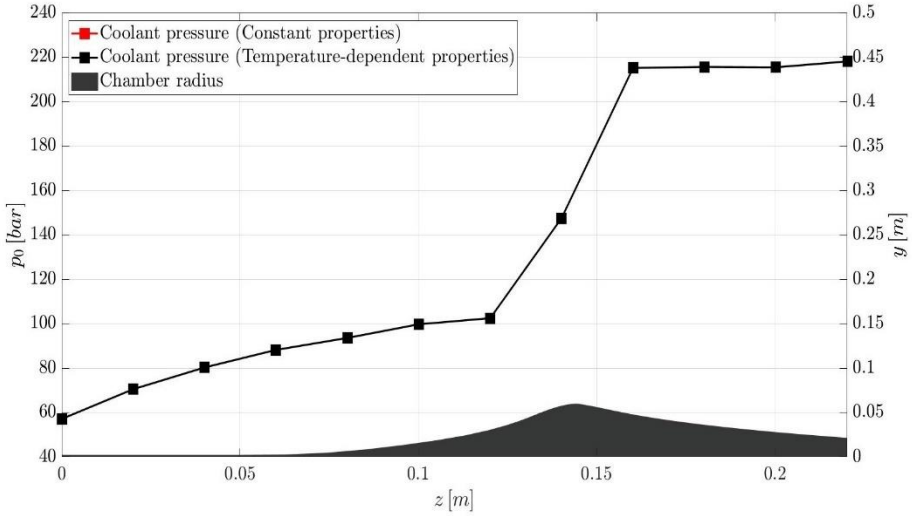

Figure 8. *Average coolant pressure at different cross-sections across longitudinal coordinate of coolant side for constant and temperature-dependent solid material properties.*

The coolant velocity of liquid oxygen in different cross-sections of the AM cooling channel is reported in Fig. 9.

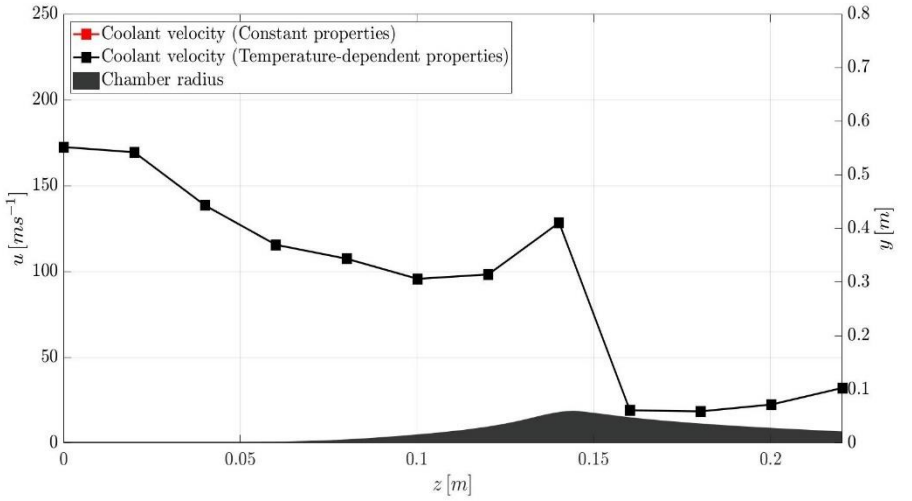

Figure 9. *Average coolant velocity at different cross-sections across longitudinal coordinate of coolant side for constant and temperature-dependent solid material properties.*

It is obvious that regardless of the constant or temperature-dependent nature of the GRCop-42 solid material properties of the DemoP1 cooling channel walls, the velocity-field is developed in a similar manner as the coolant is heated from the basement wall. The coolant enters the AM channel with a low velocity of approximately 30 [ms^{-1}] and it notably accelerates within the throat region. This behavior can be attributed to the reduction of cross-section area and fluidic width to manage the increased heat transfer load at the throat region of the cooling channel (Rossi et al., 2021). After exiting the throat region, a small deceleration of the coolant is observed and the flow gains momentum as it proceeds in the remaining, smoother part of the cooling channel towards the outlet section.

Lastly, details on the coolant density of liquid oxygen as it flows across the heated additively manufactured cooling channel of the DemoP1 aerospike engine demonstrator are reported. As it can be seen from Fig. 10 the behavior is similar for the cases where constant and temperature-dependent solid material properties for GRCop-42 are employed for the wall boundaries of the AM cooling channel. The density of the coolant is reduced across the channel with an adverse reduction of the density property observed at the throat region. Different heat transfer phenomena may arise from this significant density reduction identified for the flow of liquid oxygen in the AM cooling channel of the DemoP1 aerospike engine demonstrator such as heat transfer deterioration, which will be investigated in future work.

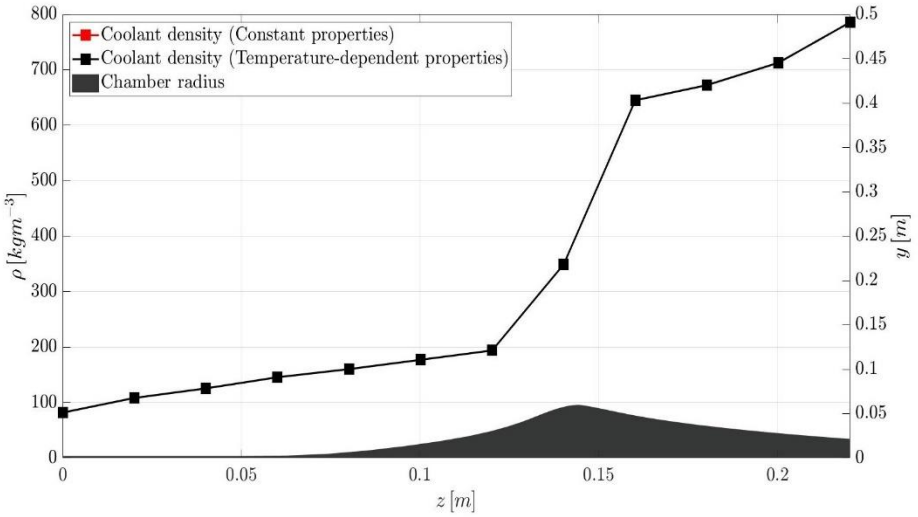

Figure 10. *Average coolant density at different cross-sections across longitudinal coordinate of coolant side for constant and temperature-dependent solid material properties.*

4. Conclusions and future work

In the present work temperature-dependent correlations have been obtained for the density, specific heat capacity at constant pressure and thermal conductivity of the copper-alloy GRCop-42 used to additively manufacture the DemoP1 aerospike engine demonstrator. The temperature-dependent solid material properties were implemented in a User-Defined Function (UDF) and introduced in the commercial CFD package employed for the performance of the required simulations. The numerical results obtained from the simulations for constant and variable solid material properties were then compared against the experimental data from the hot-flow test of the DemoP1 aerospike engine demonstrator. This study focuses on presenting new correlations for the description of the thermophysical properties of the novel

copper-based alloy GRCop-42 and their application for the investigation of their capability to provide a realistic physical description of the material behavior in high heat flux aerospace applications.

The numerical simulation performed using constant GRCop-42 solid material properties exhibits good agreement with the measurement obtained from the hot-flow experimental campaign of the DemoP1 engine. It is shown that both the imposition of constant with temperature and temperature-dependent solid material properties for the GRCop-42 material on the wall boundaries produce similar results for the resolved averaged variables of interest for the liquid oxygen flow in the AM cooling channel of the DemoP1 aerospike engine demonstrator. The employment of variable thermophysical properties for the copper-based alloy is found to have no actual improvement on the numerical solution of the liquid oxygen flow in the AM cooling channel. This can be attributed to a number of reasons such as the resolution of the near-wall region and the internal boundary layer. It is important to notice that in high roughness flows the viscous sublayer is altered by the non-uniformly distributed rough elements inherited by the AM process on the surfaces of the cooling channel. In a way the resolution of the roughness sublayer and the disruption of the viscous sublayer from the rough elements is expected to poorly capture the effect of the variable thermophysical properties upwind of the surrounding wall boundaries and up to the outer region of the boundary layer, especially in an averaged manner such as the one performed in this analysis. In addition, the steady-state Reynolds-Averaged Navier-Stokes (RANS) computational fluid dynamics approach selected may not be able to capture significant deviations in the averaged quantities of the variables of interest for the liquid oxygen flow between the performed simulations in order to properly identify the influence of different approaches for the solid material properties. Lastly, further to the numerical uncertainty of the performed simulations, consideration should be given on the uncertainty resulting from the experimental measurements utilised for the regression models employed in this study. Data for the implementation of the thermal boundary condition and the thermophysical properties of GRCop-42 were fitted using regression analysis.

The results of this study indicate the necessity to perform higher fidelity analysis for the resolution of the near-wall region to accurately capture the influence of the temperature-dependent solid material properties on the flow characteristics. Future work will include the implementation of different roughness resolution methods. Apart from the consideration of the roughness effects through the modification of the RANS boundary conditions, the roughness resolving approach where the geometrical features and scales of the actual rough elements are explicitly included will also be employed in conjunction with three-dimensional scale resolving simulations to improve the accuracy of the numerical solution. For this reason, three-dimensional scale resolving simulations for the investigation of the effect of the variable GRCop-42 alloy thermophysical properties on the liquid oxygen flow in the AM cooling channel of the DemoP1 aerospike engine demonstrator will be a topic of future work. Different roughness resolution methods will also be a topic of future work.

5. Acknowledgements

The present research work was financially supported by the Centre for Propulsion and Thermal Power Engineering and the Cranfield Air and Space Propulsion Institute (CASPI) at Cranfield University, UK in collaboration with Pangea Aerospace, Spain. The authors would also like to acknowledge the IT support and the use of the High Performance Computing (HPC) facilities at Cranfield University, UK.

6. Data availability statement

The data that support the findings of this study are available from the corresponding author upon request.

7. Conflict of interest statement

The authors declare no conflict of interest.

References

[1] Ansys Fluent User's Guide. ANSYS 2023 R2. Ansys Inc., Canonsburg, PA, 2023.

[2] Betti, B., Pizzarelli, M., & Nasuti, F. (2014). Coupled heat transfer analysis in regeneratively cooled thrust chambers. *Journal of Propulsion and Power*, *30*(2), 360–367. **https://doi.org/10.2514/1.B34855**

[3] Cahill, J. A., & Kirshenbaum, A. D. (1962). The density of liquid copper from its melting point (1356°K.) to 2500°K and an estimate of its critical constants. *The Journal of Physical Chemistry*, *66*(6), 1080–1082. **https://doi.org/10.1021/j100812a027**

[4] Chase, M. W., Jr. (1998). NIST-JANAF Thermochemical Tables, Fourth Edition. *Journal of Physical and Chemical Reference Data*, Monograph 9, 1-1951.

[5] Chen, Y., Zeng, C., Ding, H., Emanet, S., Gradl, P. R., Ellis, D. L., & Guo, S. (2023). Thermophysical properties of additively manufactured (AM) GRCop-42 and GRCop-84. *Materials Today Communications*, *36*, 106665.

https://doi.org/10.1016/j.mtcomm.2023.106665

[6] Cooper, K. G., Lydon, J. D., LeCorre, M. D., Jones, Z. C., Scannapieco, D. S., Ellis, D. L., & Lerch, B. A. (2018). Three-dimensional printing GRCop-42. *NASA Technical Memorandum (TM)*. NASA.

[7] Demeneghi, G., Barnes, B., Gradl, P. R., Mayeur, J. R., & Hazeli, K. (2021). Size effects on microstructure and mechanical properties of additively manufactured copper-chromium-niobium alloy. *Materials Science and Engineering A*, *820*, 141511.

https://doi.org/10.1016/j.msea.2021.141511

[8] Demin, M., Koroleva, O., Aleksashkina, A., & Mazhukin, V. (2020). Molecular-dynamic modeling of thermophysical properties of phonon subsystem of copper in wide temperature range. *Mathematica Montisnigri*, *47*, 137–151. **https://doi.org/10.20948/mathmontis-2020-47-12**

[9] Deprés, D., Reijasse, P., & Dussauge, J. P. (2004). Analysis of unsteadiness in afterbody transonic flows. *AIAA Journal*, *42*(12), 2541–2550. **https://doi.org/10.2514/1.7000**

[10] Ellis, D. L. (2004). *Conductivity of GRCop-42 Alloy Enhanced*. NASA.

[11] Ellis, D. L. (2005). GRCop-84: A high-temperature copper alloy for high-heat-flux applications. *NASA Technical Memorandum (TM)*. NASA.

[12] Fadigati, L., Rossi, F., Souhair, N., Ravaglioli, V., & Ponti, F. (2024). Development and simulation of a 3D printed liquid oxygen/liquid natural gas aerospike. *Acta Astronautica*, *216*, 105–119. **https://doi.org/10.1016/j.actaastro.2023.12.037**

[13] Ghidini, T., Grasso, M., Gumpinger, J., Makaya, A., & Colosimo, B. M. (2023). Additive manufacturing in the new space economy: Current achievements and future perspectives. *Progress in Aerospace Sciences*, *142*, 100959. **https://doi.org/10.1016/j.paerosci.2023.100959**

[14] Gibson, I., Rosen, D., & Stucker, B. (2015). Directed Energy Deposition Processes. *Additive Manufacturing Technologies: 3D Printing, Rapid Prototyping, and Direct Digital Manufacturing*. Springer New York (NY). **https://doi.org/10.1007/978-1-4939-2113-3**

[15] Gradl, P. R.: *Rapid fabrication techniques for liquid rocket channel wall nozzles*, 2016 52nd AIAA/SAE/ASEE Joint Propulsion Conference. **https://doi.org/10.2514/6.2016-4771**

[16] Gradl, P. R., Mireles, O. R., Katsarelis, C., Smith, T. M., Sowards, J., Park, A., Chen, P., Tinker, D. C., Protz C. S., Teasley, T., Ellis, D. L., & Kantzos, C. (2023). Advancement of extreme environment additively manufactured alloys for next generation space propulsion applications. *Acta Astronautica*, *211*, 483–497. **https://doi.org/10.1016/j.actaastro.2023.06.035**

[17] Gradl, P. R., Protz, C. S., Cooper, K., Ellis, D. L., Evans, L. J., & Garcia, C. (2019). GRCop-42 development and hot-fire testing using additive manufacturing Powder Bed Fusion for channel-cooled combustion chambers. *AIAA Propulsion and Energy 2019 Forum*. **https://doi.org/10.2514/6.2019-4228**

[18] Gradl, P. R., Protz, C., Greene, S. E., Ellis, D. L., Lerch, B., & Locci, I.: *Development and hot-fire testing of additively manufactured copper combustion chambers for liquid rocket engine applications*, 2017 53rd AIAA/SAE/ASEE Joint Propulsion Conference. **https://doi.org/10.2514/6.2017-4670**

[19] Ho, C. Y., Powell, R. W., & Liley, P. E. (1972). Thermal conductivity of the elements. *Journal of Physical and Chemical Reference Data*, *1*(2), 279–421. **https://doi.org/10.1063/1.3253100**

[20] Jasthi, B. K., Kuca, T. S., Ellingsen, M. D., Ellis, D. L., Kandadai, V. A. S., & Curtis, T. R. (2023). Microstructure and mechanical properties of cold spray additive manufactured Cu-Cr-Nb and Fe-Ni-Cr alloys. *Additive Manufacturing*, *61*, 103354.

https://doi.org/10.1016/j.addma.2022.103354

[21] Jian, D., & Qiuru, Z. (2020). Key technologies for thermodynamic cycle of precooled engines: A review. *Acta Astronautica*, *177*, 299–312. **https://doi.org/10.1016/j.actaastro.2020.07.039**

[22] Kerstens, F., Cervone, A., & Gradl, P. R. (2021). End to end process evaluation for additively manufactured liquid rocket engine thrust chambers. *Acta Astronautica*, *182*, 454–465. **https://doi.org/10.1016/j.actaastro.2021.02.034**

[23] Kozyrev, N. V. (2023). Thermodynamic properties and equation of state for solid and liquid copper. *International Journal of Thermophysics*, *44*, 31. **https://doi.org/10.1007/s10765-022-03136-4**

[24] Landes, S., Suresh, T., Prasad, A., Letcher, T., Gradl, P. R., & Ellis, D. L. (2020). Investigation of additive manufactured GRCop-42 alloy developed by Directed Energy Deposition methods. *Proceedings of the ASME 2020 International Mechanical Engineering Congress and Exposition. Volume 4: Advances in Aerospace Technology*. **https://doi.org/10.1115/IMECE2020-24400**

[25] Li, W.-Y., Guo, X. P., Verdy, C., Dembinski, L., Liao, H. L., & Coddet, C. (2006). Improvement of microstructure and property of cold-sprayed Cu–4 at.%Cr–2 at.%Nb alloy by heat treatment. *Scripta Materialia*, *55*(4), 327–330. **https://doi.org/10.1016/j.scriptamat.2006.04.041**

[26] Menter, F. R. (1994). Two-equation eddy-viscosity turbulence models for engineering applications. *AIAA Journal*, *32*(8), 1598–1605. **https://doi.org/10.2514/3.12149**

[27] Menter, F. R. (2009). Review of the shear-stress transport turbulence model experience from an industrial perspective. *International Journal of Computational Fluid Dynamics*, *23*(4), 305–316. **https://doi.org/10.1080/10618560902773387**

[28] Morshed-Behbahani, K., Aliyu, A., Bishop, D. P., & Nasiri, A. (2024). Additive manufacturing of copper-based alloys for high-temperature aerospace applications: A review. *Materials Today Communications*, *38*, 108395. **https://doi.org/10.1016/j.mtcomm.2024.108395**

[29] National Institute of Standards and Technology (NIST). (2023). *NIST Standard Reference Database Number 69*. NIST Chemistry WebBook. **https://doi.org/10.18434/T4D303**

[30] Pizzarelli, M., Nasuti, F., & Onofri, M. (2013). Coupled wall heat conduction and coolant flow analysis for liquid rocket engines. *Journal of Propulsion and Power*, *29*(1), 34–41. **https://doi.org/10.2514/1.B34533**

[31] Ricci, D., Natale, P., & Battista, F. (2016). Experimental and numerical investigation on the behavior of methane in supercritical conditions. *Applied Thermal Engineering*, *107*, 1334–1353. **https://doi.org/10.1016/j.applthermaleng.2016.07.052**

[32] Roe, P. L. (1981). Approximate Riemann solvers, parameter vectors, and difference schemes. *Journal of Computational Physics*, *43*(2), 357–372. **https://doi.org/10.1016/0021-9991(81)90128-5**

[33] Rossi, F., Esnault, G., Sápi, Z., Palumbo, N., Argemí, A., & Bergström, R.: *Research activities in the development of DemoP1: A LOX/LNG aerospike engine demonstrator*, 2021 7th Edition of the Space Propulsion Conference, Virtual.

[34] Rossi, F., Sápi, Z., Palumbo, N., Demediuk, A., & Ampudia, M.: *Manufacturing and hot-fire test campaign of the DemoP1 aerospike engine demonstrator*, 2022 8th Edition of the Space Propulsion Conference, Estoril, Portugal.

[35] Saltzman, D., Bichnevicius, M., Lynch, S., Simpson, T. W., Reutzel, E. W., Dickman, C., & Martukanitz, R. (2018). Design and evaluation of an additively manufactured aircraft heat exchanger. *Applied Thermal Engineering*, *138*, 254–263.

https://doi.org/10.1016/j.applthermaleng.2018.04.032

[36] Scharnowski, S., & Kähler, C. J. (2021). Investigation of the base flow of a generic space launcher with dual-bell nozzle. *CEAS Space Journal*, *13*, 197–216.

https://doi.org/10.1007/s12567-020-00333-5

[37] Simon, N. J., Drexler, E. S., & Reed, R. P. (1992). *Properties of copper and copper alloys at cryogenic temperatures*. Final report. United States. **https://doi.org/10.2172/5340308**

[38] Statnikov, V., Sayadi, T., Meinke, M., Schmid, P., & Schröder, W. (2015). Analysis of pressure perturbation sources on a generic space launcher after-body in supersonic flow using zonal turbulence modeling and dynamic mode decomposition. *Physics of Fluids*, *27*(1), 016103. **https://doi.org/10.1063/1.4906219**

[39] Tang, X., Chen, X., Sun, F., Liu, P., Zhou, H., & Fu, S. (2022). The current state of CuCrZr and CuCrNb alloys manufactured by additive manufacturing: A review. *Materials & Design*, *224*, 111419. **https://doi.org/10.1016/j.matdes.2022.111419**

[40] The MathWorks, I. (2020). *Curve Fitting Toolbox*. Natick, Massachusetts, United States. https://www.mathworks.com/products/curvefitting.html

[41] Thurnay, K. (1998). Thermal properties of transition metals. Materials Science, Physics, Chemistry. **https://doi.org/10.5445/IR/270043419**

[42] Tsentis, S., Goulos, I., Prince, S., Pachidis, V., & Zmijanovic, V. (2023). Propulsion aerodynamics for a novel high-speed exhaust system. *ASME Journal of Engineering for Gas Turbines and Power*, *145*(12), 121011. **https://doi.org/10.1115/1.4063416**

[43] Tsentis, S., Goulos, I., Prince, S., Pachidis, V., Zmijanovic, V., & Saavedra, J. (2024). Wind tunnel installation effects on the base flow for a high-speed exhaust system. AIAA SCITECH 2024 Forum. **https://doi.org/10.2514/6.2024-1774**

[44] White, G. K., & Collocott, S. J. (1984). Heat capacity of reference materials: Cu and W. *Journal of Physical and Chemical Reference Data*, *13*(4), 1251–1257. **https://doi.org/10.1063/1.555728**

[45] Weiss, P.-É, Deck, S., Robinet, J.-C., & Sagaut, P. (2009). On the dynamics of axisymmetric turbulent separating/reattaching flows. *Physics of Fluids*, *21*(7), 075103. **https://doi.org/10.1063/1.3177352**